Check for updates

ARTICLE

Tertiary lymphoid structures correlate with enhancement of antitumor immunity in esophageal squamous cell carcinoma

Shoichi Nakamura[1], Kenoki Ohuchida [1][✉], Masataka Hayashi[1], Naoki Katayama[1], Chikanori Tsutsumi[1], Yutaka Yamada[2], Kyoko Hisano[1], Sho Okuda[1], Yoshiki Ohtsubo[1], Chika Iwamoto[1,3], Nobuhiro Torata[1], Yusuke Mizuuchi[1], Koji Shindo[1], Kohei Nakata[1], Taiki Moriyama[1], Takashi Morisaki[4], Yoshinao Oda[2] and Masafumi Nakamura[1]

BACKGROUND: Tertiary lymphoid structures (TLSs) are associated with a favorable prognosis in several cancers. However, the correlation between TLSs and outcomes of esophageal squamous cell carcinoma (ESCC) and the impact of TLSs on the tumor immune microenvironment (TIME) remain unknown.
METHODS: We pathologically evaluated the significance of TLSs in ESCC focusing on TLS maturation using 180 ESCC specimens and performed single-cell RNA sequencing (scRNA-seq) using 14 ESCC tissues to investigate functional differences of immune cells according to TLS presence.
RESULTS: TLS+ cases had better recurrence-free-survival (RFS) ($p < 0.0001$) and overall survival (OS) ($p = 0.0016$) compared with TLS- cases. Additionally, mature TLS+ cases had better RFS and OS compared with immature TLS+ cases ($p = 0.019$ and $p = 0.015$) and TLS- cases ($p < 0.0001$ and $p = 0.0002$). The scRNA-seq showed that CD8$^+$ T cells in TLS+ tumors expressed high levels of cytotoxic signatures and antigen-presentation of dendritic cells (DCs) was enhanced in TLS+ tumors. Immunohistochemistry showed that the densities of tumor-infiltrating CD8$^+$ T cells and DCs were significantly higher in TLS+ tumors than those in TLS- tumors.
CONCLUSIONS: These data suggest the prognostic and functional significance of TLSs in ESCC and provides new insights into TLSs on the TIME.

BACKGROUND

Esophageal cancer was the sixth leading cause of cancer-related mortality worldwide in 2020 [1]. The main histological type of esophageal cancer is esophageal squamous cell carcinoma (ESCC), which has a high morbidity rate in Southeast Asia [1]. While multimodal therapy for ESCC in available, the prognosis of ESCC patients remains poor [2]. Recently, several clinical trials reported the efficacy of immune checkpoint blockage (ICB) for ESCC [3, 4]. ICB response is known to depend on the tumor immune microenvironment (TIME) [5]. Moreover, various types of immune cells in the TIME play key roles in carcinogenesis and tumor progression. However, the functional roles of each type of immune cell in the ESCC TIME have been unclear because of their complicated heterogeneity. Better understanding of the TIME is urgently required to improve the effectiveness of immunotherapy in ESCC.

Recently, many publications focused on tertiary lymphoid structures (TLSs) in the TIME, which may play a crucial role in immunotherapy [6]. TLSs are ectopic lymphoid formations that develop in non-lymphoid sites of chronic inflammation, auto-immune diseases and tumors and represent lymphoid neogenesis in response to prolonged exposure to inflammatory signals with

chemokines and cytokines [7]. Similar to secondary lymphoid structures, TLSs are composed of several immune cells, including T cells, B cells, dendritic cells (DCs), follicular dendritic cells (FDCs), fibroblast reticular cells and endothelial cells [8]. Germinal centers (GCs) in TLSs are important sites of B cell clonal expansion and antibody affinity maturation. They consist of several cell types, such as germinal center B cells (GCBs), centroblasts, centrocytes, follicular helper T cells (Tfh cells) and FDCs [9]. High endothelial venules (HEVs) are detected around TLSs and correlate with tumor-infiltration of T cells and B cells [10]. Recent studies showed that TLSs perform various functions in the TIME. Mature DCs in TLSs are associated with cytotoxic effector functions of CD8$^+$ T cells and a favorable prognosis in non-small cell lung cancer [11]. T cells within TLSs upregulate the expression of activation genes, such as *CD27* and *GZMB* [12]. B cells in GCs show clonal amplification, somatic mutation and isotype switching and indicate an antigen-specific B cell response in TLSs [13]. Antigen-presenting B cells locate in GCs of TLSs and induce antitumor T cell responses [14]. Although TLSs were reported to promote antitumor immunity, it remains insufficient to evaluate comprehensively how the TLSs influence on the TIME. Additionally, TLS presence correlates with a favorable prognosis and the

---

[1]Department of Surgery and Oncology, Graduate School of Medical Sciences, Kyushu University, Fukuoka, Japan. [2]Department of Anatomic Pathology, Graduate School of Medical Sciences, Kyushu University, Fukuoka, Japan. [3]Department of Hematology, Clinical Immunology and Infectious Diseases, Graduate School of Medicine, Ehime University, Ehime, Japan. [4]Department of Cancer Immunotherapy, Fukuoka General Cancer Clinic, Fukuoka, Japan. ✉email: ouchida.kenoki.060@m.kyushu-u.ac.jp

efficacy of ICBs in many cancer types, including breast cancer [15], pancreatic cancer [16], colorectal cancer [17] and gastric cancer [18]. However, the significance of TLSs in ESCC remains unknown.

Single-cell RNA sequencing (scRNA-seq) provides new opportunities to systematically characterize the heterogeneity of immune cells in the TIME at the single-cell level. While conventional bulk RNA-sequencing tools analyze millions of cells with averaging out the heterogeneity of each cell, scRNA-seq can evaluate differences of each individual cell type. The characterization of functional heterogeneity of immune cells using scRNA-seq has been reported in several cancers, such as breast cancer [19], pancreatic cancer [20], colorectal cancer [21], gastric cancer [22] and ovarian cancer [23]. A recent study in ESCC using scRNA-seq showed the landscape of epithelial cells, including tumor cells and non-malignant epithelial cells, and revealed that immune checkpoint genes, such as LAG3 and HAVCR2, were expressed significantly more highly in ESCC tissues than in normal tissues [24]. Another report revealed that the tumor-infiltration of myofibroblasts, which is one subtype of fibroblasts, was increased in ESCC tissues compared with that in normal tissues [25]. However, there have been few studies reporting transcriptome characterization in the ESCC TIME at the single-cell level, and no reports have focused on TLS presence in ESCC tissues using scRNA-seq.

In this study, we evaluated the relationship between TLS presence and prognosis in ESCC patients, with a focus on the maturation of TLSs. We performed scRNA-seq with ESCC tissues categorized by TLS presence and evaluated the functional differences in each type of immune cell composing the TIME between TLS+ and TLS- tumors. These data showed how mature TLSs enhance antitumor immunity in the TIME and suggested that TLSs could be a novel therapeutic target to improve the efficacy of immunotherapy and outcomes of ESCC.

MATERIALS AND METHODS
ESCC patient cohort
This study cohort included patients who underwent surgical resection and histopathologic diagnosis for ESCC in the Department of Surgery and Oncology, Kyushu University Hospital between 2008 and 2020. The study protocols were approved by the Kyushu University Certified Institutional Review Board for Clinical Trials (#22002-00). Several cases with microscopic residual tumors and without any tumors after endoscopic treatments were excluded. In total, 180 tumor samples were analyzed in this study. The clinicopathological characteristics of patients are listed in Supplementary Table S1.

FFPE co-detection by indexing (CODEX) multiplexed tissue imaging
CODEX imaging was conducted as previously described [26]. Briefly, 4 μm–thick FFPE sections were rehydrated and heat-induced epitope retrieval was performed. The sections were stained with a DNA-conjugated antibodies and imaged following the protocols of Akoya Biosciences. Primary antibodies are described in Supplementary Table S2. Imaging was performed using an optical microscope (BZX-810; Keyence, Osaka, Japan), an Akoya CODEX microfluidics instrument (Akoya Biosciences, Menlo Park, CA, USA), CODEX instrument management software (v1.29.3.6) and CODEX processor software (v1.7). We evaluated images with Fiji/ImageJ (National Institutes of Health, https://fiji.sc/, v1.53c, RRID: SCR_002285).

TLS definition
TLSs were determined using both H&E and IHC staining for CD20 in FFPE sections by a pathologist (YY) and an analyst (SN) who were blinded to the outcomes of ESCC patients. The TLS classification was defined morphologically by the following three types of maturation as previously described [12, 27]: i) Negative (Neg): no existence of TLSs around tumors; ii) Aggregates (Agg): vague and ill-defined clusters of lymphocytes without segregated T and B cell zones; and iii) Follicles (Fl): round shaped large clusters of lymphocytes. GCs are aggregated structures of immune cells that exhibit a characteristic morphology of proliferating centroblasts

in TLSs, as previously reported [28]. Using this classification, we observed TLSs in ESCC specimens and classified cases as follows: i) Neg-ESCC: tumors without any TLSs; ii) Agg-ESCC: tumors with only Agg and no Fl; iii) Fl-ESCC: tumors with at least one Fl structure. Agg-ESCC cases were additionally stained using CD3 antibody to confirm that T cells were clustered in the same location as B cell aggregations. We categorized Neg-ESCC as TLS-, and Agg-ESCC and Fl-ESCC were categorized as TLS+, as reported previously [27, 29]. Univariate and multivariate analyses with TLS presence in ESCC patients were shown in Table S3.

Patient specimens for scRNA-seq
Human patient samples for scRNA-seq were collected with written informed consent and ethics approval by Kyushu University Certified Institutional Review Board for Clinical Trials (#2022-100). Written informed consent was provided by all patients prior to this study. Patient metadata are provided as Supplementary Table S4. Patient age varied from 41 to 80 years.

scRNA-seq library preparation and sequencing
Fresh tumors and normal mucosae after surgery were dissociated for sequencing. We performed experiments following an online protocol (https://doi.org/10.17504/protocols.io.b2udqes6). scRNA-seq library preparations were carried out using the Chromium Next GEM Single Cell 3′ GEM, Library & Gel Bead Kit v3.1 (10x Genomics, Pleasanton, CA, USA, #PN-1000121) following the manufacturer's protocol. A total of 8,000 viable cells were used per sample. These scRNA-seq samples were sequenced on DNBSEQ-G400 (MGI Tech, Shenzhen, China) or Illumina NovaSeq 6000 (Illumina, San Diego, CA, USA).

Processing of scRNA-seq data
Raw sequencing reads were aligned to the human genome (GRCh38) using 10× Cell Ranger analysis pipeline (ver. 5.0.0) to generate barcode matrices. The gene-barcode matrices were processed using Seurat R package (ver. 3.6.3). Low quality cells with >10% unique molecular identifiers mapped to mitochondrial transcripts and >5000 expressed genes were excluded.

scRNA-seq data analysis
We normalized the processed data and identified 2000 features with high cell-to-cell variation in the dataset. To mitigate the effects of cell cycle heterogeneity in scRNA-seq data, we calculated cell-cycle phase scores based on canonical markers, assigned each cell a score using "CellCycleScoring" and subtracted heterogeneity from the data. Principal components analysis (PCA) was performed on the integration-transformed expression matrix to reduce dimension. We refined edge weights between any two cells based on the shared overlap in the PCA using "FindNeighbors" and clustered the cells using "FindCluster." We then ran non-linear dimensional reduction to visualize integrated and lineage specific datasets using Uniform Manifold Approximation and Projection (UMAP).

Evaluation of gene signatures
To evaluate the potential functions of cell-subtypes of interest, we defined function-related gene signatures and investigated the expression of signatures. The involved gene signatures are listed in Supplementary Table S5.

Differentially expressed genes (DEGs) and pathway enrichment analysis
DEGs were analyzed by TLS presence using a two-sided Wilcoxon rank-sum test with Bonferroni FDR collection. To gain functional insights of the DC subtype, we performed Gene Ontology (GO) pathway enrichment analyses using Metascape (https://metascape.org/gp/index.html#/main/step1, RRID: SCR_016620) [30]. The top 100 DEGs using the "FindMarkers" tool with the DC subtype were imported to Metascape.

NicheNet and trajectory analyses workflow
The NicheNet workflow referred to the protocols described at https://github.com/saeyslab/nichenetr [31]. During NicheNet runs, the Tfh subtype and the GCB subtype were set as 'sender' clusters and the DC subtype was set as 'receiver' cluster. DEGs enriched in TLS+ compared with TLS- in the DC subtype were identified as target receptor genes. The NicheNet

workflow was performed using the protocol to predict ligands connecting target receptors and create a Circos plot visualizing ligand-receptor interactions for cell-types of interest. Trajectory analyses were run with Monocle3 on Seurat objects [32].

Immunohistochemistry and multiplex immunofluorescence

FFPE specimens were cut as 4 μm–thick sections; these sections were deparaffined in xylene and hydrated through an ethanol series. Endogenous peroxidase activity was blocked by methanol with 0.3% hydrogen peroxidase (15 min). To retrieve antigen-epitope, the slides were boiled for 20 min in Citrate Buffer (pH 5.9) or Tris-EDTA Buffer (pH 9.0). Unspecific binding sites were masked with PBS + 3% BSA for 15 min. Slides were incubated with primary antibodies at 4 °C overnight. The primary antibodies were as follows: Bcl6 (Abcam, Cambridge, UK, # ab249707, 1:100), CD4 (R&D Systems, Minneapolis, MN, USA, # AF-379-NA, 1:200, RRID: AB_354469), CD8 (Abcam, #ab4055, 1:200, RRID:AB_304247), CD20 (Nichirei, Tokyo, Japan, #422441, 1:100), CD11c (EP1347Y; Abcam, #ab52632, 1:500, RRID: AB_2129793) and IGKC (Santa Cruz Biotechnology, CA, USA, #sc-59264, 1:100, RRID: AB_783962). Slides were rinsed and incubated with secondary antibody (DAKO/Agilent, Glostrup, Denmark, Rabbit, K4003, and Mouse, K4001) for 1 h at room temperature. Nuclei were counterstained with hematoxylin (Muto Pure Chemicals Co., Ltd, Tokyo, Japan, #30002). For immunohistochemistry, staining was developed with a 3,3′-diaminobenzidine kit (Sigma-Aldrich, Darmstadt, Germany, #D5537-5G). For immunofluorescence staining, specimens were incubated with secondary antibodies in PBS + 0.1% BSA for 1 h at room temperature. Secondary antibodies for immunofluorescence were as follows: Donkey-anti-rabbit-AF488, Donkey-anti-mouse-AF546 and Donkey-anti-goat-AF647 (Invitrogen, Massachusetts, USA, 1:200); nuclei were stained with DAPI (1:1000). Fluorescence images were acquired with an optical microscope (BZ-X800; Keyence).

Evaluation of immunohistochemistry and immunofluorescence imaging

Immunohistochemical staining was analyzed by a pathologist (YY) and an analyst (SN) who were blinded to the clinical characteristics and outcomes of the patients. We counted positive cells of each marker at high power field. The data were expressed as a density (total number of positive cells per mm^2). We used H&E staining to evaluate the location and extent of the tumor bed. We then examined tumor-infiltrating immune cells using immunohistochemical staining. For detection of SEMA4D$^+$ Tfh cells, we identified mature TLSs using multiple immunofluorescences staining and counted the number of CD4$^+$ cells, CD4$^+$SEMA4D$^+$ cells and CD4$^+$SEMA4D$^+$Bcl6$^+$ cells (CD4$^+$Bcl6$^+$ cells: Tfh cells). Data were expressed as a proportion of CD4$^+$ T cells. Imaging analyses were performed using an optical microscope (BZ-X800) and ImageJ. Images were acquired with BZ-X800 and cells were counted manually using ImageJ.

Statistics

Statistical analyses were performed using GraphPad Prism (GraphPad Software, San Diego, CA, USA, v9.3.1, RRID: SCR_002798) or JMP software (SAS Institute, Cary, NC, USA, v16.0.0, RRID: SCR_008567). Survival analysis was performed by Cox proportional hazards model and survival curves (RFS and OS) were performed by the Kaplan–Meier method and compared with the log-rank test. Chi-square test or Fisher's exact test were used to evaluate the correlations between clinicopathological characters and TLS presence (Supplementary Table S1). Dunn's multiple comparisons test was used for comparisons of histological types with cell proportions in ESCC. We performed Cox proportional hazard analyses using JMP software and used GraphPad Prism for other statistical analyses. The Wilcoxon rank-sum test was performed to compare proportions of several immune cell types, the expression of specific genes and gene signatures and the numbers of CD8$^+$ cells, IGKC$^+$ cells, CD11c$^+$ cells, and SEMA4D$^+$ Tfh cells. All statistical tests were two-sided and $p < 0.05$ indicated statistical significance.

RESULTS
TLS presence predicts a favorable prognosis in ESCC
To detect TLSs in ESCC tissues, we examined ESCC samples from 180 ESCC patients who underwent surgical resection using hematoxylin and eosin (H&E) staining, CD3 and CD20

immunohistochemical staining (Supplementary Table S1). Most TLSs were found at the invasive margin of tumors (Fig. 1a). We classified TLSs into three types of maturation: i) Negative (Neg); ii) Aggregates (Agg); iii) Follicles (Fl) (see Materials and Methods, Fig. 1a, b, Supplementary Fig. S1A and Supplementary Table S2). Moreover, many FL-cases contained GCs. GCs consisted of several cell types, such as characteristic B cell subtypes (centroblasts and centrocytes) and FDCs, as previously reported [33] (Supplementary Fig. S1B). The degree of TLS maturation was Neg, Agg and Fl in 36 (20.0 %), 37 (20.6 %) and 107 (59.4 %) cases, respectively. ESCC cases without TLSs were categorized as "TLS-" cases, and cases with TLSs were categorized as "TLS + " cases (see Materials and Methods). TLS- and TLS+ were detected in 36 (20.0 %) and 144 (80.0 %) cases, respectively. We investigated the correlations between TLS presence and clinicopathologic characteristics (Supplementary Table S1). We found that TLS presence correlated positively with lower T stage ($p = 0.0196$), absence of lymph node metastasis ($p = 0.0294$) and lower TNM stage ($p = 0.0029$). We investigated the prognostic values of TLS presence using Kaplan–Meier curves and found that TLS+ cases had better recurrence-free-survival (RFS) ($p < 0.0001$) and overall survival (OS) ($p = 0.0016$) compared with TLS- cases (Fig. 1c, d). As TLSs mature, a GC is formed and immune responses are promoted in the GC [34]. We next investigated the impact of TLS maturation on prognosis and found that Fl-cases had better RFS and OS compared with Agg-cases ($p = 0.019$ and $p = 0.015$) and Neg-cases ($p < 0.0001$ and $p = 0.0002$) (Fig. 1e, f). We further performed univariate and multivariate analyses with clinicopathological features (Supplementary Table S3). Univariate Cox regression analyses showed that T stage, lymph node metastasis and TLS presence were significantly correlated with RFS in ESCC (hazard ratio (HR) = 0.44, 95% confidence interval (CI): 0.26–0.76, $p = 0.003$; HR = 0.32, 95% CI: 0.17–0.60, $p = 0.0005$; HR = 0.35, 95% CI: 0.20–0.61, $p = 0.0002$, respectively) and lymph node metastasis and TLS presence were significantly correlated with OS in ESCC (HR = 0.39, 95% CI: 0.18–0.82, $p = 0.013$; HR = 0.35, 95% CI: 0.17–0.69, $p = 0.0027$, respectively). Multivariate Cox regression analyses revealed that lymph node metastasis and TLS presence were independent prognostic factors for RFS (HR = 0.40, 95% CI: 0.20–0.80, $p = 0.0092$; HR = 0.42, 95% CI: 0.23–0.75, $p = 0.0032$, respectively) and TLS presence was an independent prognostic factor for OS (HR = 0.38, 95% CI: 0.19–0.78, $p = 0.0079$). A recent study reported TLS subtypes with different localizations, such as peritumoral TLSs and intratumoral TLSs [35]. In the present study, we also examined FL-cases and grouped them into two subtypes on the basis of TLS location (Supplementary Fig. S1C). We found few cases of intratumoral TLSs in our patient cohort (5.9%). Kaplan–Meier curves showed no significant differences in RFS and OS between peritumoral and intratumoral TLSs ($p = 0.0624$ and $p = 0.1349$) (Supplementary Fig. S1D). These data suggest that TLS presence and maturation were correlated with a favorable prognosis in ESCC.

Single-cell transcriptome defines the cellular composition of ESCC samples
To evaluate differences in the TIME in accordance with TLS presence at the single-cell level, we analyzed 14 ESCC samples (10 tumor tissues and 4 normal tissues) using scRNA-seq (Supplementary Fig. S2A and Supplementary Table S4). After quality control, the dataset included 71,116 total cells. After normalization with gene expression, we identified 25 distinct cell clusters with graph-based clustering on the principal components analysis (PCA) (Supplementary Fig. S2B). The major cell types were annotated by canonical lineage markers (Supplementary Fig. S2C, D). Each case was then categorized by TLS presence using H&E staining and CD20 staining of FFPE specimens. The clusters were represented across each case
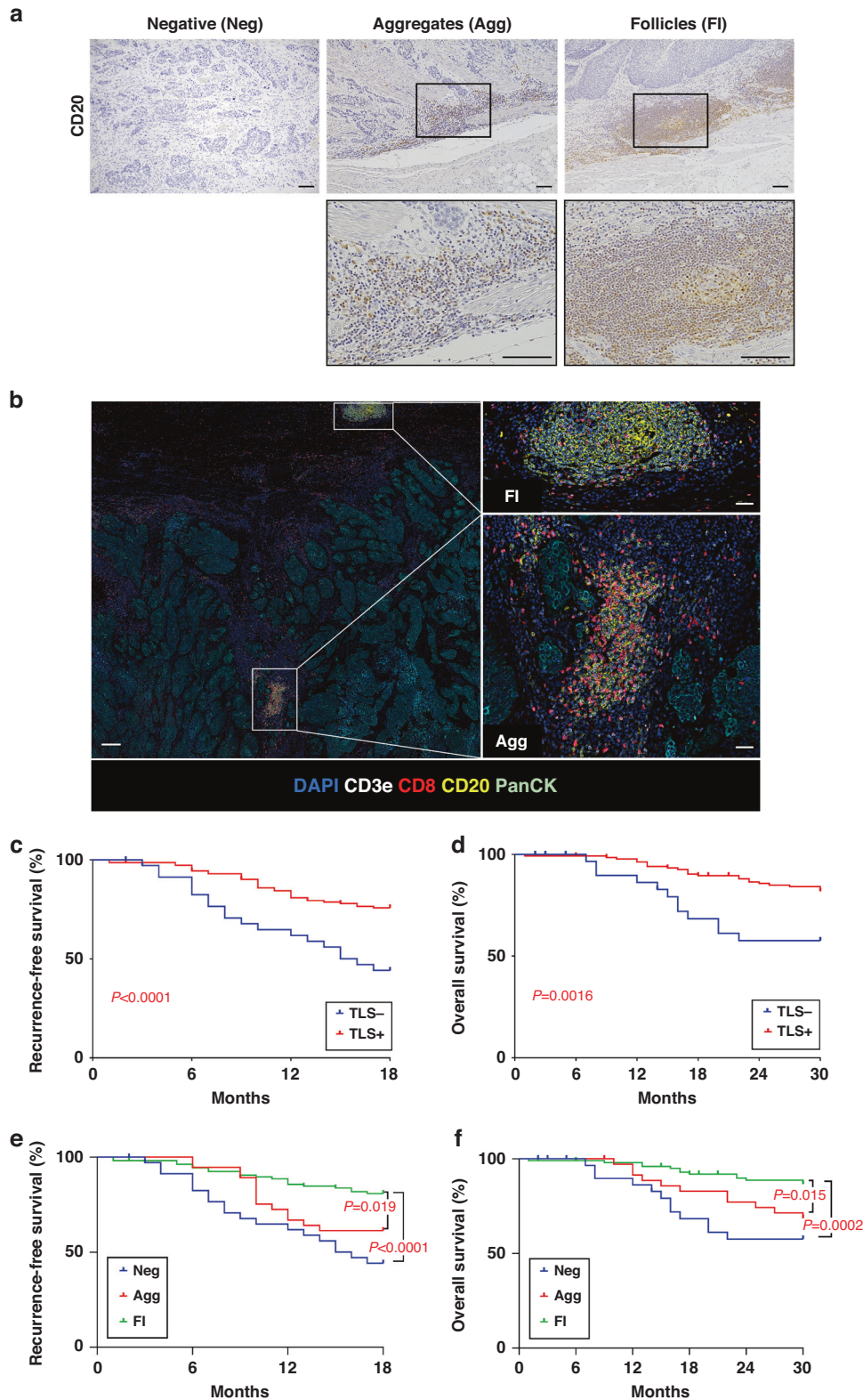
Fig. 1 The TLS classification and the relationship between TLSs and a prognosis in ESCC patients. a Representative images of IHC staining of CD20 showing TLSs (Negative (Neg), Aggregates (Agg) and Follicles (Fl)) (×100). The inset shows a higher magnification image of the boxed area. Scale bars, 100 μm. **b** CODEX multiple staining images showed TLSs. Five-color composite CODEX multiple staining images of DAPI, CD3e, CD8, CD20 and PanCK and high magnification (right). Regions of interest were shown in the white box (Fl, top; Agg, bottom). Scale bars, 1000 μm (left panel) and 200 μm (right panel). **c–f** Kaplan–Meier analyses of recurrence-free survival (RFS) and overall survival (OS) in ESCC by TLS presence or TLS maturation classification (Neg, Agg and Fl). RFS cohort: TLS- (n = 36), TLS+ (n = 144); Neg (n = 36), Agg (n = 37), Fl (n = 107). OS cohort: TLS- (n = 32), TLS+ (n = 138); Neg (n = 32), Agg (n = 36), Fl (n = 102). P values were calculated by log-rank test.
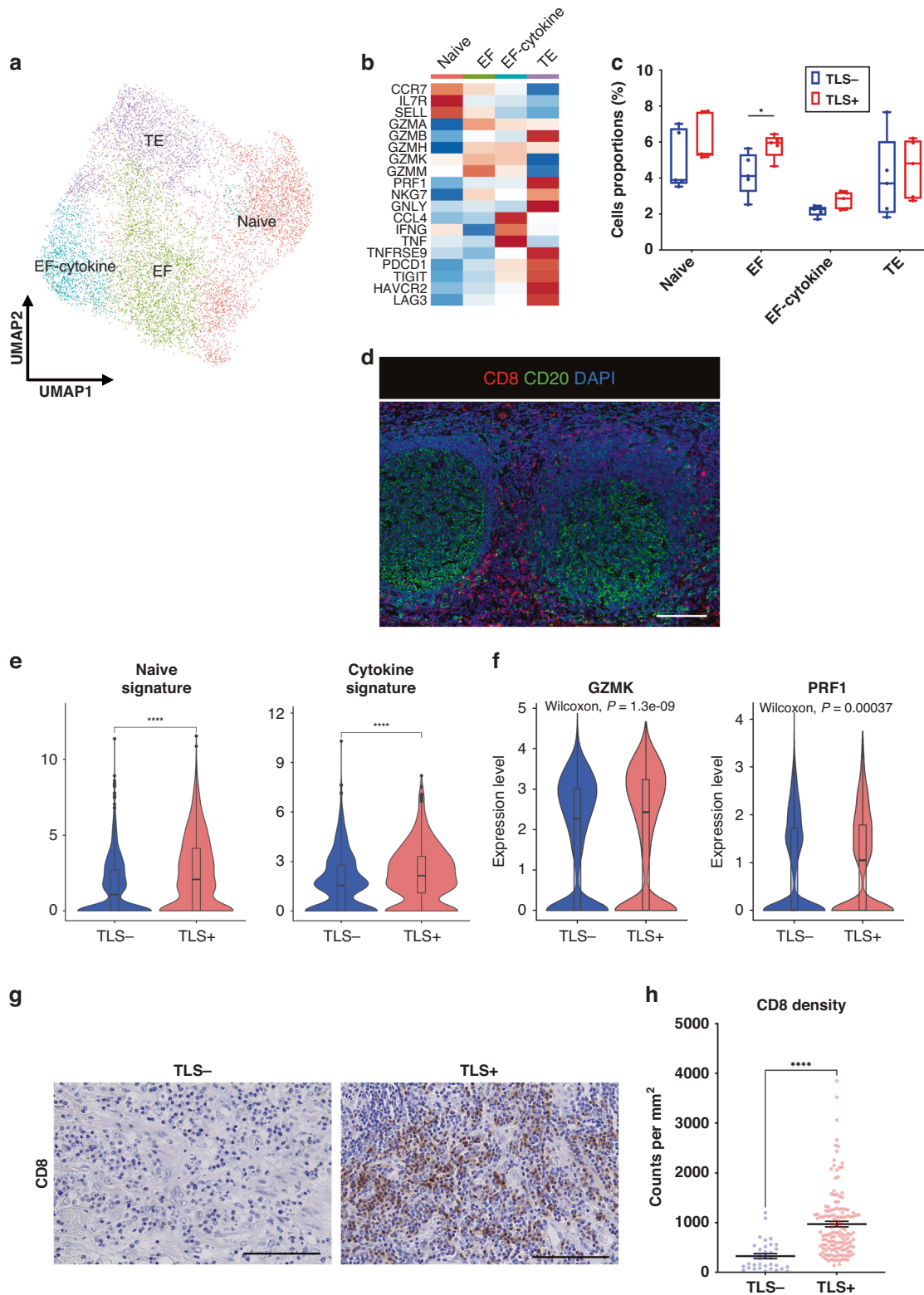
(Supplementary Fig. S2E). The proportion of fibroblasts in TLS+ tumors was significantly less than that in normal tissues ($p = 0.0076$), whereas the proportion of T cells in TLS+ tumors was significantly more than that in normal tissues ($p = 0.0050$) (Supplementary Fig. S2F). These data suggested that the proportions of cell types were different depending on the tissue type and TLS presence.

CD8+ T cells upregulate the expression of cytotoxic-related genes in TLS+ tumors

At first, we extracted the CD8+ T cell cluster to examine the heterogeneity of CD8+ T cells. After reclustering, CD8+ T cells were divided into four subtypes: naive CD8+ T cells (Naive, *CCR7*, *IL7R* and *SELL*), effector T cells (EF, *GZMA*, *GZMB*, *GZMH*, *GZMK,* and *GZMM*), effector T cells expressing cytokine-related genes

Fig. 2 CD8$^+$ T cells enhance several functions and enrich tumor-infiltration in TLS+ tumors. a UMAP plot was color-coded by four subtypes of CD8$^+$ T cells on the basis of representative genes. **b** Heatmap indicated the representative genes in each CD8$^+$ T cell subtype. **c** Box and whisker plots showed the CD8$^+$ T cell subtype distributions in accordance with TLS presence. Box middle lines, median; box limits, upper and lower quartiles; box whiskers, 1.5× the interquartile range. Wilcoxon rank-sum test was performed. *$p < 0.05$. **d** Representative immunofluorescence staining of TLSs for CD8 (red), CD20 (green) and DAPI (blue) (×200). Scale bars, 100 μm. **e** Violin plots showed the expressions of naive signature in the Naive subtype and cytokine signature in the EF-cytokine subtype in accordance with TLS presence. Significance of the gene set enrichment (p value) in accordance with TLS presence was determined by Wilcoxon rank-sum test. Boxplots included centerline, median; box limits, upper and lower quartiles; whiskers at most 1.5× the interquartile range past upper and lower quartiles. ****$p < 0.0001$. **f** Violin plots showed the expression of *GZMK* and *PRF1* in CD8$^+$ T cells in accordance with TLS presence. Significance of the gene expression (p value) in accordance with TLS presence was determined by Wilcoxon rank-sum test. Boxplots included centerline, median; box limits, upper and lower quartiles; whiskers at most 1.5× the interquartile range past upper and lower quartiles. **g** Representative images of CD8 immunohistostaining on tumor tissues in accordance with TLS presence (×400). Scale bars, 100 μm. **h** Graph showed the quantification of CD8$^+$ T cell density in tumors. Patients were divided groups in accordance with TLS presence. Mean ± SEM were shown. Wilcoxon rank-sum test was performed. ****$p < 0.0001$.

(EF-cytokine, *CCL4, IFNG,* and *TNF*) and terminally exhausted T cells (TE, *TNFRSF9, PDCD1, TIGIT, HAVCR2* and *LAG3*) (Fig. 2a, b). In the trajectory analysis, we observed the transition from the Naive subtype to the EF subtype (Supplementary Fig. S3). The proportion of the EF subtype was significantly larger in TLS+ tumors than that in TLS- tumors ($p = 0.0317$) (Fig. 2c). We investigated the localization of CD8$^+$ T cells in the TIME using multiplex immunofluorescence (mIF) staining and found that CD8$^+$ T cells were frequently located along the outer edge of TLSs, but not inside TLSs (Fig. 2d).

We next evaluated the differences in several functions of CD8$^+$ T cell subtypes in accordance with TLS presence. The Naive signature was significantly enriched in the Naive subtype, and the cytokine signature was upregulated in the EF-cytokine subtype in TLS+ tumors compared with that in TLS- tumors (Fig. 2e and Supplementary Table S5). CD8$^+$ T cells showed significantly upregulated cytotoxic-genes, such as *GZMK* and *PRF1* in TLS+ tumors compared with those in TLS- tumors (Fig. 2f). We then assessed tumor samples histologically to investigate the relationship between TLS presence and the density of tumor- infiltrating CD8$^+$ T cells. The density was significantly higher in TLS+ tumors than that in TLS- tumors ($p < 0.0001$) (Fig. 2g, h).

DCs enhance antigen-presentation in TLS+ tumors
Next, we analyzed DCs to evaluate the functional differences between TLS+ and TLS- tumors. First, after extracting the myeloid cluster, we classified five subtypes of myeloid cells: CD16-monocytes (CD16-Mono, *FCN1,* and *VCAN*), CD14-monocytes (CD14-Mono, *IFITM2,* and *LST1*), SPP1-macrophages (SPP1-Macro, *SPP1,* and *VEGFA*), FOLR2-macrophages (FOLR2-Macro, *MARCO, C1QA,* and *FOLR2*) and DCs (*XCR1* and *CLEC9A*) (Fig. 3a, b). Myeloid subtypes showed no differences in their relative abundance in accordance with TLS presence (Fig. 3c). The phenotype of myeloid cells is heterogeneous in the TIME [36]. Several phenotypes of myeloid cells, such as tumor-associated macrophages (TAMs) and myeloid-derived suppressor cells (MDSCs) have been proposed. While TAMs and MDSCs are regarded as separate phenotypes, the boundaries between them are not clearly separated and there is no representative marker to distinguish clearly between TAMs and MDSCs [37]. To characterize these subtypes, we then evaluated the enrichment of signatures, such as DC-like, MDSC-like and TAM-like signatures. CD16-Mono and CD14-Mono subtypes expressed the MDSC-like signature, whereas SPP1-Macro and FOLR2-Macro subtypes expressed the TAM-like signature (Supplementary Fig. S4A). To survey the differentiation trajectory of the cell states, we performed a pseudotime trajectory analysis. The results showed that the CD14-Mono subtype might be the progenitor of maturation in myeloid cells (Fig. 3d). To detect where DCs are located in TLSs, we used mIF staining and found that most DCs were located inside the GC of TLSs (Fig. 3e). We evaluated the functional differentiations of DCs between TLS+ and TLS- tumors and found enrichment of characteristic signatures associated with

DC activation, DC migration and antigen-presentation in TLS+ tumors compared with those in TLS- tumors (Fig. 3f). Gene Ontology (GO) enrichment analysis showed that differentially expressed genes (DEGs) in DCs within TLS+ tumors were enriched for antigen processing- and presentation-related pathway (Fig. 3g). We next focused on the density of tumor-infiltrating DCs in the TIME, because the DC migration signature was upregulated in TLS+ tumors. We found that TLS+ tumors had a significantly higher density of tumor-infiltrating CD11c$^+$ DC cells than TLS- tumors ($p < 0.0001$) (Fig. 3h and Supplementary Fig. S4B).

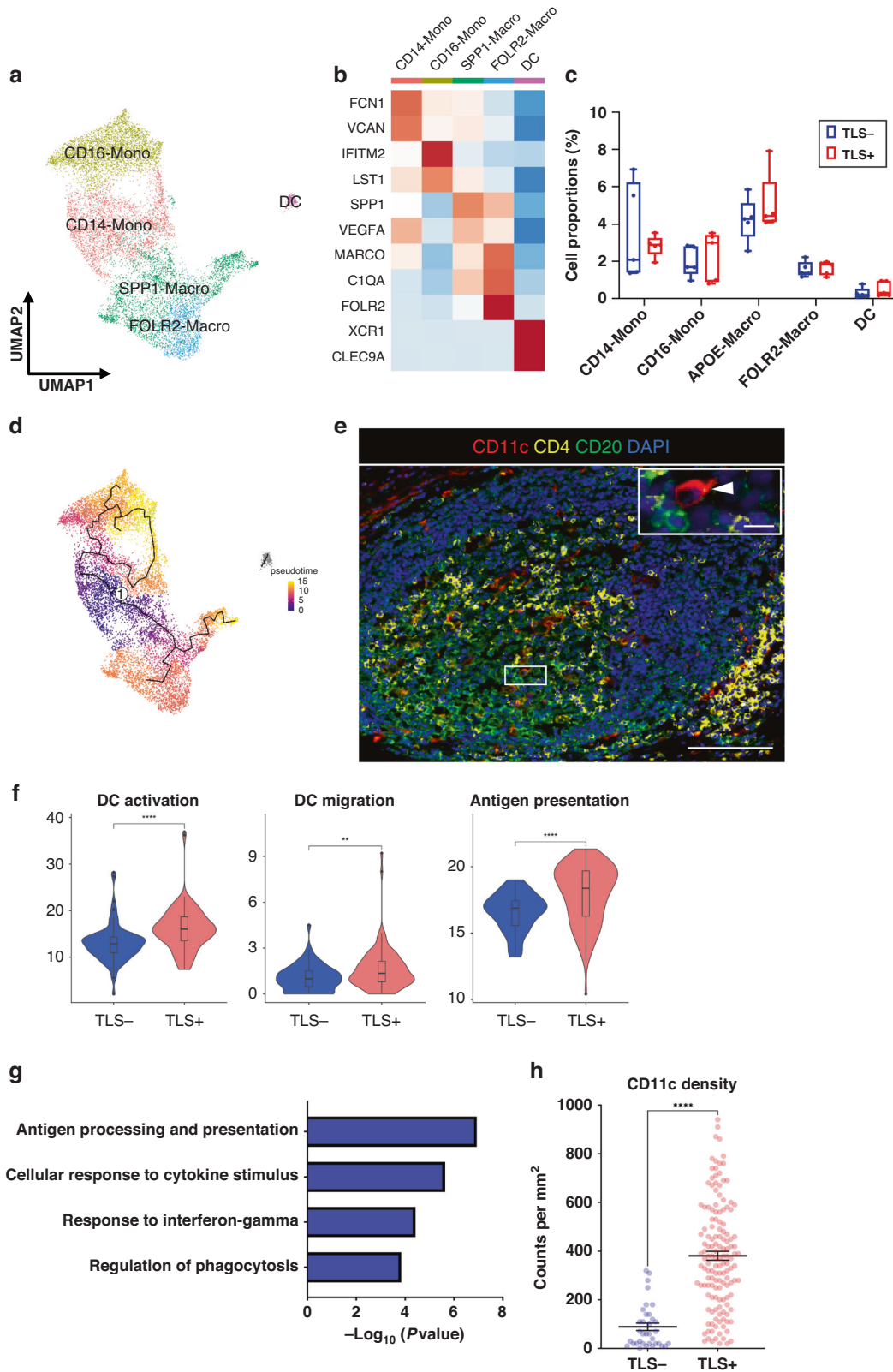**Tfh cells upregulate the expression of GC reaction-related genes in TLS+ tumors**
To investigate the functional heterogeneity of CD4$^+$ T cells in the ESCC TIME, we reclustered CD4$^+$ T cells using scRNA-seq data and identified four subtypes: naive CD4$^+$ T cells (Tn, *IL7R, CCR7, TCF7* and *LEF1*), regulatory T cells (Treg, *FOXP3* and *IL2RA*), type1 helper T cells (Th1, *TNF, IFNG* and *TBX21*) and Tfh cells (*CXCR5* and *BCL6*) (Fig. 4a, b). There was a significantly higher proportion of Tfh cells in TLS+ tumors than in TLS- tumors ($p = 0.0079$) (Fig. 4c). We observed Tfh cells (CD4$^+$Bcl6$^+$ cells) inside the GC of TLSs (Fig. 4d). To characterize the functional differences of Tfh cells between TLS+ tumors and TLS- tumors, we performed DEG analyses. High expressions of GC reaction-related genes such as *BCL6, CXCR5, CXCL13, PDCD1, ICOS,* and *CD48* [38] were found in Tfh cells in TLS+ tumors (Fig. 4e, f). These results suggested that the GC reaction in Tfh cells was promoted in TLS+ tumors.

Maturation of B cells into ASCs is promoted in TLS+ tumors
Next, we reclustered the merge data to identify B cells and classified four subtypes: naive B cells (NBCs, *IGHD* and *TCL1A*), MBCs (*ITGB1, FCRL4, CD86* and *ITGAX*), germinal center B cells (GCBs, *AICDA, RGS13* and *GCSAM*) and ASCs (*XBP1, PRDM1, IGHG1* and *IGKC*) (Fig. 5a, b). We found that GCBs were significantly enriched in TLS+ tumors versus TLS- tumors ($p = 0.0238$) (Fig. 5c). We then found that the expression levels of GCB and ASC signatures were upregulated in B cells derived from TLS+ tumors (Fig. 5d). To evaluate the relationship between TLS presence and ASC density in tumors, we used IHC staining and found that the density of tumor-infiltrating IGKC-positive cells (an ASC marker [39]) was significantly higher in TLS+ tumors than that in TLS-tumors ($p < 0.0001$) (Fig. 5e, f). These data suggested that the maturation of B cells into ASCs was promoted in TLS+ tumors.

Tfh cell-derived SEMA4D stimulates DCs in TLSs
To gain further insight into the interactions of the immune cells composing TLSs, we investigated the cross-talk among DCs, Tfh cells and GCBs using NicheNet [31]. In this analysis, we used DEGs in DCs associated with TLSs to predict key genes in Tfh cells and GCBs modulating the DEGs (see Materials and Methods). The NicheNet analysis revealed that *SEMA4D* was one of key ligands inferred to regulate several DEGs in DCs, and the Circos plot

a

UMAP2
UMAP1

CD16-Mono
CD14-Mono
SPP1-Macro
FOLR2-Macro

b

CD14-Mono
CD16-Mono
SPP1-Macro
FOLR2-Macro
DC

FCN1
VCAN
IFITM2
LST1
SPP1
VEGFA
MARCO
C1QA
FOLR2
XCR1
CLEC9A

DC

c

Cell proportions (%)

TLS−
TLS+

CD14-Mono CD16-Mono APOE-Macro FOLR2-Macro DC

d

pseudotime
15
10
5
0

e

CD11c CD4 CD20 DAPI

f

DC activation
****

DC migration
**

Antigen presentation
****

TLS− TLS+

g

Antigen processing and presentation
Cellular response to cytokine stimulus
Response to interferon-gamma
Regulation of phagocytosis

−Log$_{10}$ (Pvalue)

h

CD11c density
****

Counts per mm^2

TLS− TLS+

showed that this gene was expressed in Tfh cells (Fig. 6a, b). The SEMA4D protein, encoded by *SEMA4D*, is a type of semaphorin molecules that is expressed on T cells and stimulates DCs to promote their maturation (Supplementary Fig. S5) [40]. Considering that our data showed that DCs in TLS+ tumors were activated

and enhanced their functions (Fig. 3f), these results suggest that SEMA4D might play important roles in activating DCs. Moreover, among CD4$^+$ T cell subtypes in the ESCC TIME, Tfh cells expressed *SEMA4D* at the highest level, and Tfh cells tended to express *SEMA4D* at higher levels in TLS+ tumors than in TLS- tumors

Fig. 3 DCs are activated and enhance antigen-presentation in TLS+ tumors. a UMAP plot was color-coded by five subtypes of myeloid cells on the basis of representative genes. **b** Heatmap indicated representative genes in each myeloid cell subtype. **c** Box and whisker plots showed the B cell subtype distributions in accordance with TLS presence. Box middle lines, median; box limits, upper and lower quartiles; box whiskers, 1.5× the interquartile range. Wilcoxon rank-sum test was performed. **d** Trajectory analysis of myeloid cells. The pseudotime trajectory was calculated with lighter colors indicating newer values. **e** Representative immunofluorescence staining of TLSs for CD11c (red), CD4 (yellow), CD20 (green) and DAPI (blue) (×200). The insets showed a higher-magnification image of the boxed area (×400). Arrowheads indicated DCs. Scale bars, 100 μm and 20 μm (inset). **f** Violin plots showed the expression of activation, migration and antigen-presentation signatures in accordance with TLS presence. Significance of the gene expression (*p* value) in accordance with TLS presence was determined by Wilcoxon rank-sum test. Boxplots included centerline, median; box limits, upper and lower quartiles; whiskers at most 1.5× the interquartile range past upper and lower quartiles. *******p* < 0.01, ****p < 0.0001. **g** Gragh showed the enriched Gene Ontology term for the top 100 signature genes in DCs with TLS using Metascape. **h** Graph showed the quantification of CD11c-positive cells in tumors. Patients were divided groups in accordance with TLS presence. Mean ± SEM were shown. Wilcoxon rank-sum test was performed. ****p < 0.0001.

(Fig. 6c, d). To determine which CD4$^+$ T cell subtype mainly expresses SEMA4D in TLSs, we investigated the expression of SEMA4D in CD4$^+$ T cells located in TLSs using mIF staining. SEMA4D-positive cells were mainly observed in TLSs and Tfh cells (CD4$^+$Bcl6$^+$ cells [41]) expressed SEMA4D more frequently than non-Tfh cells (Fig. 6e, f).

DISCUSSION
In this study, we first identified the relationship between the presence and the maturation of TLSs and a favorable outcome of ESCC patients. We then evaluated the functions of the tumor-infiltration of immune cells by TLS presence with multimodal approaches, including scRNA-seq, IHC and mIF staining. Immune cell types, such as T cells, DCs and B cells, increased their antitumor immune functions in TLS+ tumors. Our results indicated that CD8$^+$ T cells enhanced cytotoxicity and DCs increased antigen-presentation in TLS+ tumors. We also found that the GC reaction in TLSs was activated and B cell maturation was promoted, and we observed the increase in tumor-infiltration of these immune cells in TLS+ tumors (Supplementary Fig. S6). These results suggest the clinical and functional significance of TLSs on immune cells in ESCC TIME and provide novel insights into how TLSs enhance antitumor immunity.

TLS presence has been reported to be a favorable prognostic factor in several solid tumors [15–18]. Many studies have reported the importance of various TLS factors for prognosis, for example the percentage area [17] and density of TLSs [42]. However, which factors associated with TLSs are important for prognosis have been unclear. In this study, we found that the maturation of TLSs was associated with improved prognosis in ESCC. As TLSs mature, segments of T and B cell zones and the GC are formed within the TLSs, and the active immune response occurs in TLSs. The maturation of TLSs also correlates with a favorable prognosis in hepatocellular carcinoma [27] and colorectal cancer [43]. Considering that mature TLSs activate antitumor immunity more than immature TLSs, evaluation of TLS maturation may be a promising tool to predict the prognosis of tumors.

The influence of TLS presence on immune cells in tumor sites had not been well known. Among several immune cell types, CD8$^+$ T cells in the TIME are powerful effectors in the antitumor response [44]. CD8$^+$ T cells release granzyme and perforin molecules to kill tumors [45] and produce high amounts of IFNγ, which enhances antitumor immunity in the TIME [46]. DCs promote immunity by presenting antigens to T cells with cell-cell contacts and cytokines and play a central role in antigen-specific immunity [47]. Therefore, we investigated the functions of CD8$^+$ T cells and DCs in the TIME classified on the basis of TLS presence. CD8$^+$ T cells in TLS+ tumors showed significantly upregulated cytokine- and cytotoxic-related signatures compared with cells in TLS- tumors. DCs enhanced the expression of genes related with antigen-presentation in TLS+ tumors. Previous studies showed that the presence of activated CD8$^+$ T cells correlated with TLS density and predicted neoantigen burden [48].

Another study reported the relationship between mature DCs in TLSs and activated CD8$^+$ T cells or a favorable prognosis [11]. Considering that TLSs are localized to tumor sites with high levels of tumor antigen exposure [7], these data suggest that DCs are effectively activated by tumor antigens in TLSs near tumors and their antigen-presentation is enhanced, possibly leading to enhancement of cytotoxic function of CD8$^+$ T cells in the TIME.

Mature TLSs have a GC containing Tfh cells and GCBs. Tfh cells enhance GC reactions in TLSs and promote B cells to differentiate into memory B cells (MBCs) and antibody-secreting cells (ASCs) [49]. We found that Tfh cells in TLS+ tumors upregulated expression levels of *ICOS* and *PDCD1*, which encodes an important co-stimulator for GC reactions with GCBs [50], and *BCL6*, which encodes a transcription factor that maintains and activates Tfh cells [51]. These data implied that Tfh cells and GCBs in TLS+ tumors activate germinal center reactions. Notably, the present data revealed that Tfh cells increased the expression of *CXCL13* in TLS+ tumors. A recent study reported that CD4$^+$ T cell-derived CXCL13 is necessary to form TLSs [52]. These data suggest that Tfh cells are activated by co-stimulation with GCBs, increase the secretion of CXCL13 and promote TLS formation. Furthermore, the present data showed that B cells upregulated ASC signatures in TLS+ tumors. Additionally, the density of tumor-infiltrating ASCs was higher in TLS+ tumors than in TLS- tumors. These data suggest that the GC reaction was promoted by GCBs in TLS+ tumors and contributed to the differentiation of B cells into ASCs.

In the present study, we focused not only on functions but also on the degree of tumor-infiltrations of immune cells. Tumor-infiltrating CD8$^+$ T cells were increased in TLS+ tumors compared with TLS- tumors and the Naive signature in CD8$^+$ T cells was upregulated in TLS+ tumors. A recent study showed that HEVs are present in TLSs and main sites of the naive CD8$^+$ T cell subtype extravasation [53]. Taken together, these data suggest that an increase of tumor-infiltrating CD8$^+$ T cells in TLS+ tumors was involved in the enhanced entry of naive T cells into tumor sites and that TLSs might promote the transformation of "cold tumors" into "hot tumors."

NicheNet analysis showed that DCs received SEMA4D signals on Tfh cells. On T cells, SEMA4D, known as CD100, stimulates DCs to enhance the expression of CD80, CD86 and MHC class II [40]. SEMA4D was reported to correlate with the tumor-infiltration of immune cells and to be a favorable prognostic marker in melanoma and bladder cancer [54]. While a previous study showed that *SEMA4D* is expressed on CD4$^+$ T cells [55], no reports have clarified which CD4$^+$ T cell subtypes in TLSs express this gene. In our study, mIF staining showed that among CD4$^+$ T cell subtypes in TLSs, Tfh cells expressed SEMA4D at the highest level. These data suggest that SEMA4D derived from Tfh cells in TLSs stimulates DCs to activate and enhance their antigen-presentations. In the TIME, it is known that there is intimate crosstalk between DCs and T cells [47]. Within TLSs, various molecules expressed by immune cells, such as SEMA4D, might activate each other and lead to sustained antitumor immunity.
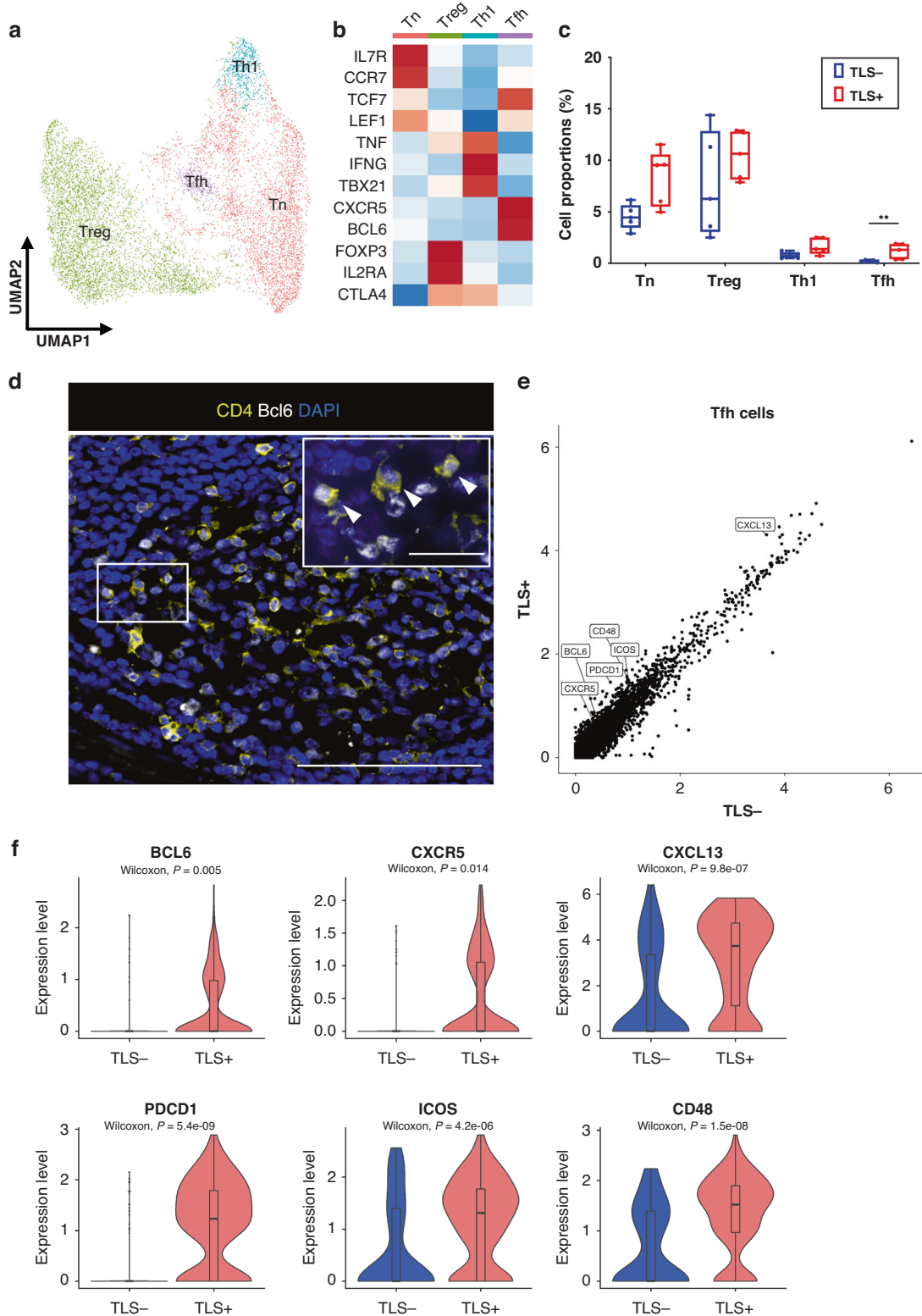
Fig. 4 **Tfh cells upregulate several TLS-related genes in TLS+ tumors. a** UMAP plot was color-coded by four subtypes of CD4$^+$ T cells on the basis of representative genes. **b** Heatmap indicated representative genes in each CD4$^+$ T cell subtype. **c** Box and whisker plots showed the CD4$^+$ T cell subtype distributions in accordance with TLS presence. Box middle lines, median; box limits, upper and lower quartiles; box whiskers, 1.5× the interquartile range. Wilcoxon rank-sum test was performed. **p < 0.01. **d** Representative immunofluorescence staining of Tfh cells in TLSs for CD4 (yellow), Bcl6 (white) and DAPI (blue) (×200). The insets showed a higher-magnification image of the boxed area (×400). Arrowheads indicated Tfh cells. Scale bars, 100 μm and 20 μm (inset). **e** Scatter plot analysis of DEGs between Tfh cells in tumors with TLS versus without TLS. **f** Violin plots showed the expression of TLS-related genes in Tfh cells in accordance with TLS presence. Significance of the gene expression (p value) in accordance with TLS presence was determined by Wilcoxon rank-sum test. Boxplots included centerline, median; box limits, upper and lower quartiles; whiskers at most 1.5× the interquartile range past upper and lower quartiles.
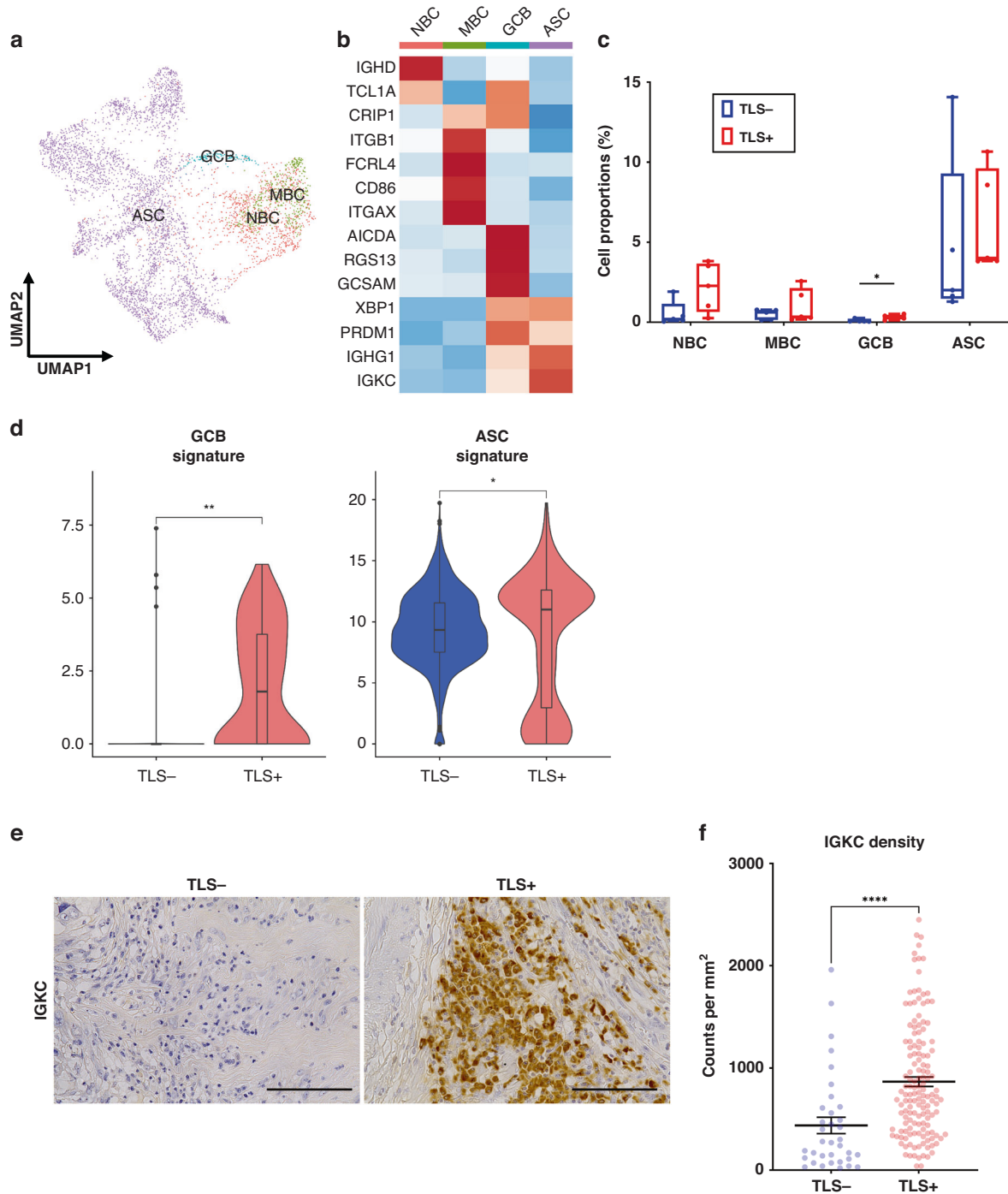
Fig. 5   B cells are promoted for maturation into ASCs in TLS+ tumors. a UMAP plot was color-coded by four subtypes of B cells on the basis of representative genes. **b** Heatmap indicated representative genes in each B cell subtype. **c** Box and whisker plots showed the B cell subtype distributions in accordance with TLS presence. Box middle lines, median; box limits, upper and lower quartiles; box whiskers, 1.5× the interquartile range. Wilcoxon rank-sum test was performed. *$p < 0.05$. **d** Violin plots showed the expression of GCB and ASC signature in accordance with TLS presence. Significance of gene expression (p value) in accordance with TLS presence was determined by Wilcoxon rank-sum test. Boxplots included centerline, median; box limits, upper and lower quartiles; whiskers at most 1.5× the interquartile range past upper and lower quartiles. *$p < 0.05$, **$p < 0.01$. **e** Representative images of IGKC immunostaining in tumor tissues with or without TLS (×400). Scale bars, 100 μm. **f** Graph showed the quantification of IGKC-positive cells in tumors. Patients were divided groups in accordance with TLS presence. Mean ± SEM were shown. Wilcoxon rank-sum test was performed. ****$p < 0.0001$.

While the clinical importance of TLS presence has been reported, its functional impact on antitumor immunity has remained unclear. This study provides new insights that TLS presence correlates with enhancement of antitumor immunity, such as enhancement of CD8+ T cell cytotoxicity and antigen-presentation of DCs. These data suggest that the induction of TLSs might be also a novel therapeutic target to promote antitumor immunity. Several studies on TLS induction have been reported. Intratumoral injection of CXCL13 and CCL21 into transplanted pancreatic tumors was shown to promote TLS induction [56]. The expression of CXCL13 in
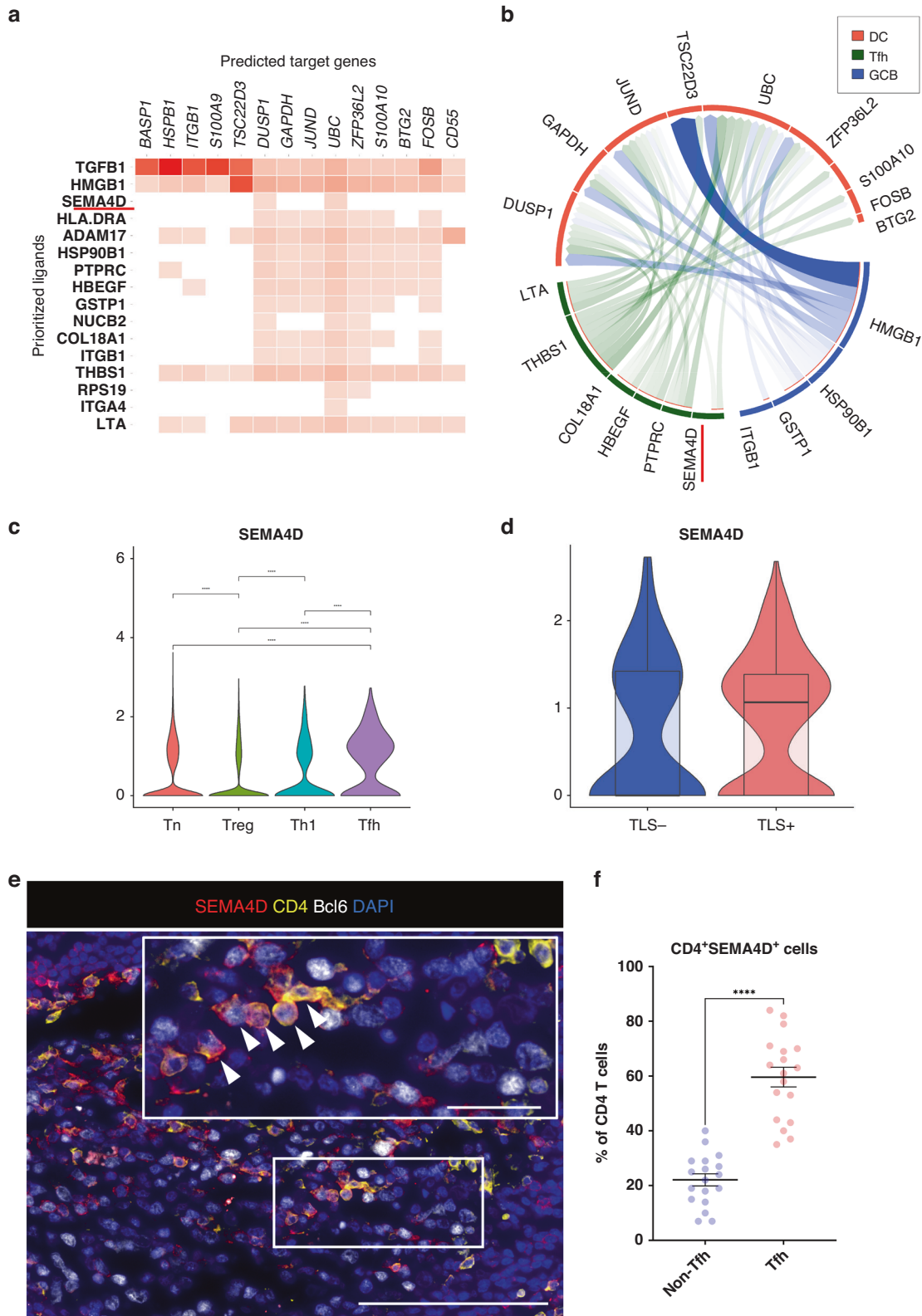
Fig. 6 ***SEMA4D* expression increases in Tfh cells in TLS+ tumors. a** Ligand activities and predicted target genes were identified by NicheNet analysis. **b** Circos plot showed the interactions between several cell types (receiver cluster, DCs; sender clusters, Tfh and GCB). **c** Violin plots showed the expression of *SEMA4D* in CD4+ T cell subtypes. Significance of gene expression (*p* value) was determined by Wilcoxon rank-sum test, with all *p*-values adjusted using Bonferroni correction. **d** Violin plots showed *SEMA4D* in Tfh cells in accordance with TLS presence. Boxplots included centerline, median; box limits, upper and lower quartiles; whiskers at most 1.5× the interquartile range past upper and lower quartiles. **e** Representative immunofluorescence staining of TLSs for SEMA4D (red), CD4 (yellow), Bcl6 (white) and DAPI (blue) (×400). Arrowheads indicated Tfh cells expressing SEMA4D. Scale bars, 100 μm and 20 μm (inset). **f** Graph showed the frequency of SEMA4D positivity on CD4+ T cells (Tfh cells or non-Tfh cells). Mean ± SEM were shown. Wilcoxon rank-sum test was performed. ****$p < 0.0001$.

pancreatic islets was reported to induce TLS formation [57]. Intratumoral injection of stimulator of interferon genes was shown to induce TLSs in a melanoma model [58]. However, the detailed mechanism of TLS induction in ESCC is not yet known. Therefore, further research is needed to identify specific cell types or molecules involved in the TLS induction of ESCC.

Moreover, the present results suggest that TLS presence, especially TLS maturation, may be a favorable prognostic marker for individualized therapy in ESCC. A recent study also reported that TLS maturation predicts ICB efficacy in solid tumors [59]. Taken together, the evaluation of TLS presence or maturation might be a promising tool to select therapeutic agents suitable for each ESCC patient.

In conclusion, we have shown that the presence of TLSs, in particular the maturation of TLSs, is correlated with a favorable prognosis in ESCC. TLSs increased tumor-infiltrating immune cells and enhanced functions associated with antitumor immunity. SEMA4D on Tfh cells stimulates DCs in TLSs. These data suggest that TLS function may be a promising therapeutic target to improve the efficacy of immunotherapy and outcomes of ESCC.

DATA AVAILABILITY
The processed scRNA-seq data were deposited in the Gene Expression Omnibus (GEO, RRID: SCR_005012) database with an accession number of GSE209524.

CODE AVAILABILITY
R script was used to analyze data and generate figures are available upon request to the corresponding authors.

REFERENCES
1. Sung H, Ferlay J, Siegel RL, Laversanne M, Soerjomataram I, Jemal A, et al. Global Cancer Statistics 2020: GLOBOCAN estimates of incidence and mortality worldwide for 36 cancers in 185 countries. CA Cancer J Clin. 2021;71:209–49.
2. Thrift AP. Global burden and epidemiology of Barrett oesophagus and oesophageal cancer. Nat Rev Gastroenterol Hepatol. 2021;18:432–43.
3. Sun J-M, Shen L, Shah MA, Enzinger P, Adenis A, Doi T, et al. Pembrolizumab plus chemotherapy versus chemotherapy alone for first-line treatment of advanced oesophageal cancer (KEYNOTE-590): a randomised, placebo-controlled, phase 3 study. Lancet. 2021;398:759–71.
4. Doki Y, Ajani JA, Kato K, Xu J, Wyrwicz L, Motoyama S, et al. Nivolumab combination therapy in advanced esophageal squamous-cell carcinoma. N Engl J Med. 2022;386:449–62.
5. Binnewies M, Roberts EW, Kersten K, Chan V, Fearon DF, Merad M, et al. Understanding the tumor immune microenvironment (TIME) for effective therapy. Nat Med. 2018;24:541–50.
6. Cabrita R, Lauss M, Sanna A, Donia M, Skaarup Larsen M, Mitra S, et al. Tertiary lymphoid structures improve immunotherapy and survival in melanoma. Nature 2020;577:561–5.
7. Sautes-Fridman C, Petitprez F, Calderaro J, Fridman WH. Tertiary lymphoid structures in the era of cancer immunotherapy. Nat Rev Cancer. 2019;19:307–25.
8. Dieu-Nosjean MC, Goc J, Giraldo NA, Sautes-Fridman C, Fridman WH. Tertiary lymphoid structures in cancer and beyond. Trends Immunol. 2014;35:571–80.
9. Victora GD, Nussenzweig MC. Germinal centers. Annu Rev Immunol. 2022;40:413–42.
10. Martinet L, Garrido I, Filleron T, Le Guellec S, Bellard E, Fournie JJ, et al. Human solid tumors contain high endothelial venules: association with T- and B-lymphocyte infiltration and favorable prognosis in breast cancer. Cancer Res. 2011;71:5678–87.
11. Goc J, Germain C, Vo-Bourgais TK, Lupo A, Klein C, Knockaert S, et al. Dendritic cells in tumor-associated tertiary lymphoid structures signal a Th1 cytotoxic immune contexture and license the positive prognostic value of infiltrating CD8+ T cells. Cancer Res. 2014;74:705–15.
12. Helmink BA, Reddy SM, Gao J, Zhang S, Basar R, Thakur R, et al. B cells and tertiary lymphoid structures promote immunotherapy response. Nature 2020;577:549–55.
13. Cipponi A, Mercier M, Seremet T, Baurain JF, Theate I, van den Oord J, et al. Neogenesis of lymphoid structures and antibody responses occur in human melanoma metastases. Cancer Res. 2012;72:3997–4007.
14. Wennhold K, Thelen M, Lehmann J, Schran S, Preugszat E, Garcia-Marquez M, et al. CD86(+) antigen-presenting B cells are increased in cancer, localize in tertiary lymphoid structures, and induce specific T-cell responses. Cancer Immunol Res. 2021;9:1098–108.
15. Gu-Trantien C, Loi S, Garaud S, Equeter C, Libin M, de Wind A, et al. CD4(+) follicular helper T cell infiltration predicts breast cancer survival. J Clin Investig. 2013;123:2873–92.
16. Hiraoka N, Ino Y, Yamazaki-Itoh R, Kanai Y, Kosuge T, Shimada K. Intratumoral tertiary lymphoid organ is a favourable prognosticator in patients with pancreatic cancer. Br J Cancer. 2015;112:1782–90.
17. Di Caro G, Bergomas F, Grizzi F, Doni A, Bianchi P, Malesci A, et al. Occurrence of tertiary lymphoid tissue is associated with T-cell infiltration and predicts better prognosis in early-stage colorectal cancers. Clin Cancer Res. 2014;20:2147–58.
18. Hennequin A, Derangere V, Boidot R, Apetoh L, Vincent J, Orry D, et al. Tumor infiltration by Tbet+ effector T cells and CD20+ B cells is associated with survival in gastric cancer patients. Oncoimmunology. 2016;5:e1054598.
19. Nalio Ramos R, Missolo-Koussou Y, Gerber-Ferder Y, Bromley CP, Bugatti M, Nunez NG, et al. Tissue-resident FOLR2(+) macrophages associate with CD8(+) T cell infiltration in human breast cancer. Cell. 2022;185:1189–207.e25.
20. Schlesinger Y, Yosefov-Levi O, Kolodkin-Gal D, Granit RZ, Peters L, Kalifa R, et al. Single-cell transcriptomes of pancreatic preinvasive lesions and cancer reveal acinar metaplastic cells' heterogeneity. Nat Commun. 2020;11:4516.
21. Becker WR, Nevins SA, Chen DC, Chiu R, Horning AM, Guha TK, et al. Single-cell analyses define a continuum of cell state and composition changes in the malignant transformation of polyps to colorectal cancer. Nat Genet. 2022;54:985–95.
22. Zhang M, Hu S, Min M, Ni Y, Lu Z, Sun X, et al. Dissecting transcriptional heterogeneity in primary gastric adenocarcinoma by single cell RNA sequencing. Gut. 2021;70:464–75.
23. Hornburg M, Desbois M, Lu S, Guan Y, Lo AA, Kaufman S, et al. Single-cell dissection of cellular components and interactions shaping the tumor immune phenotypes in ovarian cancer. Cancer Cell. 2021;39:928–44.e6
24. Chen Z, Zhao M, Liang J, Hu Z, Huang Y, Li M, et al. Dissecting the single-cell transcriptome network underlying esophagus non-malignant tissues and esophageal squamous cell carcinoma. EBioMedicine. 2021;69:103459.
25. Shi K, Li Y, Yang L, Zhang Z, Guo D, Zhang J, et al. Profiling transcriptional heterogeneity of epithelium, fibroblasts, and immune cells in esophageal squamous cell carcinoma by single-cell RNA sequencing. FASEB J. 2022;36:e22620.
26. Black S, Phillips D, Hickey JW, Kennedy-Darling J, Venkataraaman VG, Samusik N, et al. CODEX multiplexed tissue imaging with DNA-conjugated antibodies. Nat Protoc. 2021;16:3802–35.
27. Calderaro J, Petitprez F, Becht E, Laurent A, Hirsch TZ, Rousseau B, et al. Intratumoral tertiary lymphoid structures are associated with a low risk of early recurrence of hepatocellular carcinoma. J Hepatol. 2019;70:58–65.
28. Silina K, Soltermann A, Attar FM, Casanova R, Uckeley ZM, Thut H, et al. Germinal centers determine the prognostic relevance of tertiary lymphoid structures and are impaired by corticosteroids in lung squamous cell carcinoma. Cancer Res. 2018;78:1308–20.
29. Li Q, Liu X, Wang D, Wang Y, Lu H, Wen S, et al. Prognostic value of tertiary lymphoid structure and tumour infiltrating lymphocytes in oral squamous cell carcinoma. Int J Oral Sci. 2020;12:24.
30. Zhou Y, Zhou B, Pache L, Chang M, Khodabakhshi AH, Tanaseichuk O, et al. Metascape provides a biologist-oriented resource for the analysis of systems-level datasets. Nat Commun. 2019;10:1523.
31. Browaeys R, Saelens W, Saeys Y. NicheNet: modeling intercellular communication by linking ligands to target genes. Nat Methods. 2020;17:159–62.
32. Cao J, Spielmann M, Qiu X, Huang X, Ibrahim DM, Hill AJ, et al. The single-cell transcriptional landscape of mammalian organogenesis. Nature 2019;566:496–502.
33. Barone F, Gardner DH, Nayar S, Steinthal N, Buckley CD, Luther SA. Stromal fibroblasts in tertiary lymphoid structures: a novel target in chronic inflammation. Front Immunol. 2016;7:477.
34. Kang W, Feng Z, Luo J, He Z, Liu J, Wu J, et al. Tertiary lymphoid structures in cancer: the double-edged sword role in antitumor immunity and potential therapeutic induction strategies. Front Immunol. 2021;12:689270.
35. Schumacher TN, Thommen DS. Tertiary lymphoid structures in cancer. Science. 2022;375:eabf9419.
36. Engblom C, Pfirschke C, Pittet MJ. The role of myeloid cells in cancer therapies. Nat Rev Cancer. 2016;16:447–62.
37. Ugel S, De Sanctis F, Mandruzzato S, Bronte V. Tumor-induced myeloid deviation: when myeloid-derived suppressor cells meet tumor-associated macrophages. J Clin Investig. 2015;125:3365–76.
38. Horiuchi S, Wu H, Liu WC, Schmitt N, Provot J, Liu Y, et al. Tox2 is required for the maintenance of GC TFH cells and the generation of memory TFH cells. Sci Adv. 2021;7:eabj1249.

39. Wouters MCA, Nelson BH. Prognostic significance of tumor-infiltrating b cells and plasma cells in human cancer. Clin Cancer Res. 2018;24:6125–35.

40. Kumanogoh A, Suzuki K, Ch'ng E, Watanabe C, Marukawa S, Takegahara N, et al. Requirement for the lymphocyte semaphorin, CD100, in the induction of antigen-specific T cells and the maturation of dendritic cells. J Immunol. 2002;169:1175–81.

41. Yoshitomi H, Ueno H. Shared and distinct roles of T peripheral helper and T follicular helper cells in human diseases. Cell Mol Immunol. 2021;18:523–7.

42. Sofopoulos M, Fortis SP, Vaxevanis CK, Sotiriadou NN, Arnogiannaki N, Ardavanis A, et al. The prognostic significance of peritumoral tertiary lymphoid structures in breast cancer. Cancer Immunol Immunother. 2019;68:1733–45.

43. Posch F, Silina K, Leibl S, Mundlein A, Moch H, Siebenhuner A, et al. Maturation of tertiary lymphoid structures and recurrence of stage II and III colorectal cancer. Oncoimmunology. 2018;7:e1378844.

44. Raskov H, Orhan A, Christensen JP, Gogenur I. Cytotoxic CD8(+) T cells in cancer and cancer immunotherapy. Br J Cancer. 2021;124:359–67.

45. Salti SM, Hammelev EM, Grewal JL, Reddy ST, Zemple SJ, Grossman WJ, et al. Granzyme B regulates antiviral CD8+ T cell responses. J Immunol. 2011;187:6301–9.

46. Matsushita H, Hosoi A, Ueha S, Abe J, Fujieda N, Tomura M, et al. Cytotoxic T lymphocytes block tumor growth both by lytic activity and IFNgamma-dependent cell-cycle arrest. Cancer Immunol Res. 2015;3:26–36.

47. Wculek SK, Cueto FJ, Mujal AM, Melero I, Krummel MF, Sancho D. Dendritic cells in cancer immunology and immunotherapy. Nat Rev Immunol. 2020;20:7–24.

48. Workel HH, Lubbers JM, Arnold R, Prins TM, van der Vlies P, de Lange K, et al. A transcriptionally distinct CXCL13(+)CD103(+)CD8(+) T-cell population is associated with B-cell recruitment and neoantigen load in human cancer. Cancer Immunol Res. 2019;7:784–96.

49. Crotty S. Follicular helper CD4 T cells (TFH). Annu Rev Immunol. 2011;29:621–63.

50. Papa I, Vinuesa CG. Synaptic Interactions in Germinal Centers. Front Immunol. 2018;9:1858.

51. Liu X, Yan X, Zhong B, Nurieva RI, Wang A, Wang X, et al. Bcl6 expression specifies the T follicular helper cell program in vivo. J Exp Med. 2012;209:1841–52. S1-24

52. Ukita M, Hamanishi J, Yoshitomi H, Yamanoi K, Takamatsu S, Ueda A, et al. CXCL13-producing CD4+ T cells accumulate in the early phase of tertiary lymphoid structures in ovarian cancer. JCI Insight. 2022;7:e157215.

53. Asrir A, Tardiveau C, Coudert J, Laffont R, Blanchard L, Bellard E, et al. Tumor-associated high endothelial venules mediate lymphocyte entry into tumors and predict response to PD-1 plus CTLA-4 combination immunotherapy. Cancer Cell. 2022;40:318–34.e9

54. Lu Q, Cai P, Yu Y, Liu Z, Chen G, Zeng Z. Sema4D correlates with tumour immune infiltration and is a prognostic biomarker in bladder cancer, renal clear cell carcinoma, melanoma and thymoma. Autoimmunity. 2021;54:294–302.

55. Suzuki K, Kumanogoh A, Kikutani H. Semaphorins and their receptors in immune cell interactions. Nat Immunol. 2008;9:17–23.

56. Delvecchio FR, Fincham REA, Spear S, Clear A, Roy-Luzarraga M, Balkwill FR, et al. Pancreatic cancer chemotherapy is potentiated by induction of tertiary lymphoid structures in mice. Cell Mol Gastroenterol Hepatol. 2021;12:1543–65.

57. Luther SA, Lopez T, Bai W, Hanahan D, Cyster JG. BLC expression in pancreatic islets causes B cell recruitment and lymphotoxin-dependent lymphoid neogenesis. Immunity. 2000;12:471–81.

58. GeurtsvanKessel CH, Willart MA, Bergen IM, van Rijt LS, Muskens F, Elewaut D, et al. Dendritic cells are crucial for maintenance of tertiary lymphoid structures in the lung of influenza virus-infected mice. J Exp Med. 2009;206:2339–49.

59. Vanhersecke L, Brunet M, Guegan JP, Rey C, Bougouin A, Cousin S, et al. Mature tertiary lymphoid structures predict immune checkpoint inhibitor efficacy in solid tumors independently of PD-L1 expression. Nat Cancer. 2021;2:794–802.